Carbon dots derived from ginger for inhibiting inflammatory osteolysis

Xiao-Feng Shi,†[a] Xin-Lin Jia, ID †[a] Zhao-Fan Wu, ID [b] Yu Zhang,[c] Xiao-Peng Chen,[a] Huan-Ming Xiong ID *[b] and Yuan-Qing Mao*[a]

Inflammatory osteolysis, driven by excessive osteoclast activation, remains a clinical challenge requiring therapies that simultaneously suppress bone resorption and inflammation. Herein, we developed ginger-derived carbon dots (G-CDs) *via* a facile hydrothermal method as a sustainable nanotherapeutic agent. The G-CDs exhibited excellent biocompatibility, potent reactive oxygen species scavenging ability, and significant anti-inflammatory effects by downregulating key cytokines such as TNF-α, IL-6, IL-1β and iNOS. Mechanistically, G-CDs inhibited RANKL-induced osteoclastogenesis by suppressing the NF-κB signaling pathway, as evidenced by reduced phosphorylation and degradation of IκBα and p65. This suppression led to decreased expression of osteoclastogenic markers (c-Fos, NFATc1, TRAP, CTSK and DC-STAMP), disrupted F-actin ring formation, and impaired bone resorption activity. In an LPS-induced mouse calvarial osteolysis model, G-CDs significantly alleviated bone destruction and osteoclast activation in a dose-dependent manner. These findings highlight G-CDs as a multifunctional and ecologically friendly nanomaterial with great potential for treating inflammatory osteolytic diseases.

1. Introduction

Inflammatory osteolysis is a severe bone disorder that manifests the pathological resorption of bone tissue driven by an inflammatory response.[1] This process primarily involves the overactivation of osteoclasts, triggered by factors such as infections, autoimmune conditions, or chronic inflammatory diseases like rheumatoid arthritis and osteomyelitis.[2–4] The patients suffer from progressive bone loss, pain, swelling, and dysfunction in affected areas.[5] Some of them even experience loss of mobility due to focal inflammatory osteolysis. Consequently, early and timely treatment is crucial to prevent irreversible bone damage and maintain the skeletal integrity.[6] Currently, treating inflammatory osteolysis remains a significant medical challenge, as therapies must simultaneously prevent bone degradation and chronic inflammation.[7,8] To inhibit bone degradation, some key molecular pathways involved in the osteoclast genesis were studied, and RANKL

inhibitors were found to be key factors for preventing bone resorption.[9] Anti-inflammatory therapies, particularly those targeting pro-inflammatory cytokines such as TNF-α and IL-6, were also explored to mitigate inflammation-induced bone loss.[10] However, these medicines and treatments are often expensive and their production processes are not environmentally friendly, failing to meet the requirements of sustainability.

Carbon dots (CDs), as a class of innovative carbon-based nanoparticles, are famous for their outstanding photoluminescence, biocompatibility, and facile functionalization, and explored widely in biomedical applications, such as bioimaging, drug delivery, and antibacterial applications.[11–14] CDs synthesized from natural biomass—such as plants, algae, wood, or agricultural waste—often exhibit intrinsic biocompatibility and low synthetic toxicity, owing to their natural origin.[15,16] Moreover, unlike conventional heavy-metal quantum dots, CDs generally show minimal cytotoxicity, making them better suited for *in vivo* use and reducing long-term accumulation risks.[17–21]

Notably, the carbonization of herbal medicines—exemplified by *Sanguisorbae Radix Carbonisata* and *Zingiberis Rhizoma Carbonisatum*—has been clinically practiced for centuries to achieve hemostatic and anti-inflammatory effects.[16,22,23] This tradition implies that carbonization can fundamentally transform the bioactive composition and therapeutic properties of herbal materials.[16] During this process, functional groups (*e.g.*, hydroxyl, carboxyl, and amino) from precursors are often retained or modified, becoming enriched on the CD surface

*[a]Shanghai Key Laboratory of Orthopaedic Implants, Department of Orthopedics, Shanghai Ninth People's Hospital, Shanghai Jiao Tong University School of Medicine, 639 Zhizaoju Road, Shanghai 200011, P. R. China.
E-mail: MAOYQ1975@sh9hospital.org.cn*
[b]Department of Chemistry, Shanghai Key Laboratory of Electrochemical and Thermochemical Conversion for Resources Recycling, Fudan University, Shanghai 200438, P. R. China. E-mail: hmxiong@fudan.edu.cn
[c]Department of Orthopedics, The First People' s Hospital of Zhumadian, Zhumadian, Henan 463000, P. R. China
† These authors contributed equally to this work.

and contributing to water dispersity, biocompatibility, and bio-interactivity—attributes that may underlie their noted anti-inflammatory and antibacterial functions.[24,25] Moreover, the reduction in material size to the nanoscale may enable CDs to participate in regulating intracellular redox homeostasis *via* electron transfer processes, thereby influencing physiological and pathological processes such as inflammation and apoptosis.[26,27]

Ginger, a widely used medicinal and edible plant, offers a compelling source for CD synthesis due to its well-established anti-inflammatory and antioxidant properties.[28,29] Rich in bioactive compounds such as [6]-gingerol, shogaols, and polysaccharides, ginger exerts anti-inflammatory effects partly through suppression of the NF-κB signaling pathway.[30,31] CDs derived from ginger (G-CDs) can inherit this high biocompatibility and safety profile, circumventing the toxicity concerns common to synthetic nanomaterials and easing the path toward clinical translation. Additionally, the abundance and low cost of ginger align well with the principles of green and sustainable nanomaterial production.

In this work, we developed uniform and well-dispersed G-CDs through a facile hydrothermal method using natural ginger as a carbon source. The resulting G-CDs effectively suppressed inflammatory cytokine expression and attenuated osteoclast differentiation, fusion, and bone resorption activity *via* modulation of the NF-κB signaling pathway. Furthermore, *in vivo* experiments demonstrated that G-CDs significantly mitigated LPS-induced inflammatory osteolysis in a mouse calvarial model. Collectively, our findings identify G-CDs as a sustainable and promising nanotherapeutic candidate for treating inflammatory osteolytic disorders.

2. Materials and methods

2.1 Materials, synthesis, and characterization

Ginger was bought from a Chinese food market. Alpha-modified minimal essential medium (α-MEM) and fetal bovine serum were supplied by Gibco-BRL (Sydney, Australia). Recombinant mouse M-CSF and RANKL were obtained from R&D Systems (Minneapolis, MN, USA). The tartrate-resistant acid phosphatase (TRAP) staining kit was procured from Sigma-Aldrich (St Louis, MO, USA) and the cell viability assay kit (CCK-8) was obtained from Dojindo Molecular Technology (Kumamoto, Japan). The Total Superoxide Dismutase (SOD) Activity Assay Kit, utilizing the WST-8 method, was commercially obtained from Beyotime Biotechnology (China).

As seen in Scheme 1, the extracted ginger juice was transferred into centrifuge tubes and centrifuged at 12 000 rounds per second for 10 min. After removal of solid residues, the clarified juice was subjected to hydrothermal treatment in an autoclave at 180 °C for 2 h. The resulting liquid was cooled naturally, and then dialyzed using a 1000 Da molecular weight cutoff (MWCO) membrane with buffer changes every 8 h. After 48 h of dialysis, the solution was filtered through a 0.22 μm filter. The purified solution was then lyophilized to obtain G-CD powder.
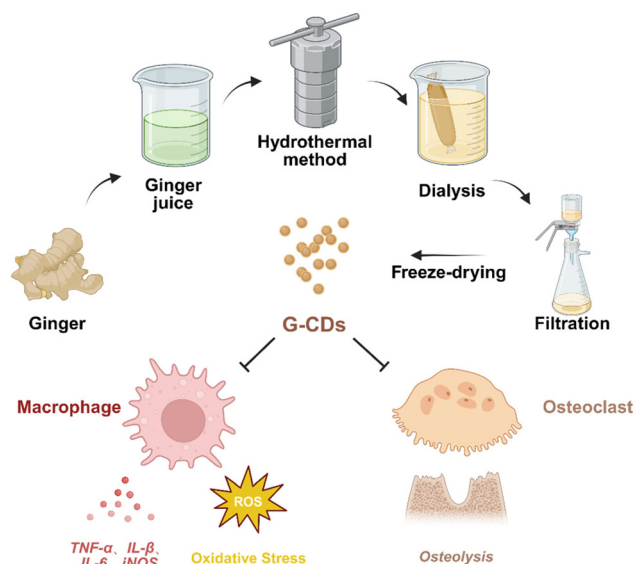
Scheme 1 The preparation route and main functions of G-CDs.

The morphology and chemical structure of the G-CDs were characterized as follows. Transmission electron microscopy (TEM) images were obtained using a Tecnai G2 F20 S-Twin electron microscope operated at 200 kV. Fourier-transform infrared (FTIR) spectroscopy was performed on a Nicolet iS10 spectrometer. Photoluminescence (PL) spectra were recorded with a Horiba Jobin Yvon FluoroMax-4 spectrofluorometer. X-ray photoelectron spectroscopy (XPS) data were collected on a Thermo ESCALAB 250Xi system, and UV–vis absorption spectra were recorded using a PerkinElmer Lambda 650S spectrophotometer.

2.2 Cell culture

Bone marrow-derived macrophages (BMMs) from specific-pathogen-free (SPF) male C57/BL6 mice were prepared and cultured in complete α-MEM with 10% fetal bovine serum (FBS), 100 U mL^{-1} penicillin/streptomycin and 35 ng mL^{-1} M-CSF, and further maintained for 5–7 days at 37 °C in a 5% CO$_2$-humidified environment to obtain mature macrophages.[7] RAW264.7 cells (a murine leukemia monocyte/macrophage line) were purchased from the American Type Culture Collection (Manassas, VA, USA) and maintained in a medium with 5% FBS and 100 U mL^{-1} penicillin/streptomycin at 37 °C under a 5% CO$_2$-humidified atmosphere. Bone marrow mesenchymal stem cells (BMSCs) were isolated from the femurs and tibias of C57BL/6 mice, flushed with complete culture medium, and then cultured in a humidified incubator at 37 °C with 5% CO$_2$. After 48 hours, non-adherent cells were removed by replacing the medium, and adherent BMSCs were expanded for subsequent experiments.

2.3 Cell viability assay

To perform the CCK-8 assay, a six-well set containing 5×10^3 BMM cells and RAW264.7 cells was plated in 96-well plates

and incubated with culture medium containing varying concentrations of G-CDs for 24 hours. Subsequently, 100 μL of fresh medium containing 10 μL of CCK-8 solution was added to each well. The plates were then incubated for an additional 2 hours at 37 °C. Following this, the optical density at 450 nm was measured using a microplate reader (Thermo, USA), with 630 nm as the reference wavelength. Cell viability was expressed as percentage relative to the vehicle-treated control cells, which were assigned a value of 100%.

2.4 Cellular uptake of G-CDs

RAW264.7 cells were seeded in confocal dishes and allowed to adhere overnight. The cells were then treated with various concentrations of G-CDs (0, 10, 50, and 100 μg mL^{-1}) for 0.5 hours at 37 °C. After incubation, the cellular uptake of G-CDs was directly visualized using a laser scanning confocal microscope (DMi8, Leica, Germany).

2.5 RNA extraction and quantitative real-time PCR analysis

Total RNA was extracted from cells using an Axygen RNA Miniprep Kit (Axygen, Union City, CA, USA). One milligram of total RNA was reverse transcribed with a PrimeScript RT Kit (Takara Biotechnology), and the resulting complementary DNA (cDNA) was used as a template for quantitative real-time PCR (qRT-PCR) assays with a TB Green Premix Ex Taq Kit (Takara Biotechnology). All reactions were performed in triplicate and normalized to the expression of the housekeeping gene GAPDH. The primers used in the experiments are listed in Table S1.

2.6 Quantifying the antioxidant potential of G-CDs

To assess the hydrogen peroxide (H_2O_2) scavenging capacity of G-CDs, a 3,3′,5,5′-tetramethylbenzidine (TMB) colorimetric assay was performed. Briefly, 50 μL of G-CDs at varying concentrations (0, 10, 50, and 100 μg mL^{-1}) were added to a 96-well plate, followed by 50 μL of TMB substrate solution (1 : 1 v/v). After thorough mixing, the reaction system was incubated at 25 °C for 20 min under light-protected conditions. The absorbance at 650 nm was immediately measured using a microplate reader (Thermo, USA).

The SOD-like enzyme activity of G-CDs was assessed both directly in a cell-free system and within RAW264.7 cells using a WST-8-based kit, following the manufacturer's protocol. For the cellular assay, RAW264.7 cells were incubated with G-CDs (0, 10, 50, and 100 μg mL^{-1}) for 24 h and then lysed after washing. For the cell-free assay, G-CDs at identical concentrations were directly employed. In both cases, the lysates or the G-CD solutions were mixed with the WST-8/enzyme working solution, incubated at 37 °C in the dark for 30 min, and the absorbance at 450 nm was measured to calculate the SOD activity.

Generation of intracellular reactive oxygen species (ROS) was evaluated using the cell-permeable fluorescent probe 2′,7′-dichlorofluorescein diacetate (DCFH-DA).[32] RAW264.7 cells grown on coverslips were stimulated with hydrogen peroxide and simultaneously co-treated with varying concentrations of G-CDs. After incubation with 10 μM DCFH-DA at 37 °C for 15 minutes, the cells were washed twice with PBS. Fluorescence images of the stained cells were then acquired using fluorescence microscopy.

2.7 OC differentiation and TRAP staining assay

To assess osteoclast differentiation, 1.0×10^4 bone marrow-derived macrophages (BMMs) were seeded in triplicate in 96-well plates and cultivated in complete α-MEM supplemented with the macrophage colony-stimulating factor (M-CSF, 35 ng mL^{-1}), receptor activator of nuclear factor κB ligand (RANKL, 50 ng mL^{-1}), and G-CDs (0, 50, and 100 μg mL^{-1}). The medium was refreshed every two days until multinucleated pie-shaped osteoclasts were observed (days 5–7). After fixation with 4% paraformaldehyde for 20 minutes, the cells were incubated in a tartrate-resistant acid phosphatase (TRAP) staining solution at 37 °C for 45 minutes. Multinucleated cells that stained positively for TRAP and contained more than three nuclei were recognized as osteoclasts. Digital images were captured using a light microscope (Olympus, Tokyo, Japan), and the number of osteoclasts and the area of cell spread were quantified using ImageJ software (National Institutes of Health, Bethesda, MD, USA).

2.8 Podosome actin belt immunofluorescence

To visualize the immunofluorescence staining of podocyte actin filaments, BMMs were continuously treated with TRAP as previously described in detail. Briefly, after the formation of mature osteoclasts, the cells were fixed with 4% paraformaldehyde for 15 minutes and permeabilized with 0.5% Triton X-100 in PBS for 5 minutes. Subsequently, the cells were incubated with rhodamine-labeled phalloidin, which was diluted in PBS containing 1% bovine serum albumin (BSA), for 30 minutes in the dark. After being thoroughly washed with PBS, the cells were counterstained with DAPI for 5 minutes to label the nuclei. Images were captured using a fluorescence microscope (Leica Microsystems), and the number and dispersion of podocyte actin bands were quantitatively analyzed with ImageJ software.

2.9 Bone resorption assay

To evaluate osteoclast-mediated bone resorption, BMMs at a density of 1×10^4 cells per well were seeded onto bovine bone slices placed in a 96-well plate. The cells were then cultured until mature osteoclasts were formed. After confirmation of OC maturation, the osteoclasts were treated with different concentrations of G-CDs (0, 50, and 100 μg mL^{-1}) for 48 hours. Subsequently, the bone slices were examined to visualize resorption pits, and images were captured using a scanning electron microscope (FEI Instruments, Hillsboro, OR, United States).

2.10 Alkaline phosphatase (ALP) staining

After osteogenic induction, the culture medium was aspirated and the BMSCs were gently rinsed with PBS (2–3 times). The BMSCs were fixed with 4% paraformaldehyde for 15 minutes

at room temperature, followed by additional PBS washes. Subsequently, the fixed cells were completely covered with an ALP staining solution and incubated in the dark at room temperature for 30 minutes. The reaction was terminated by removing the staining solution and thoroughly rinsing with PBS. ALP-positive cells, identified by the presence of blue/purple precipitates, were observed under a microscope.

2.11 Western blotting analysis

BMMs were plated in 6-well plates (3×10^5 cells per well) and stimulated with M-CSF (35 ng mL^{-1}), RANKL (50 ng mL^{-1}), and varying OSC medium doses. Proteins were subsequently extracted with RIPA buffer (Sigma-Aldrich) according to the protocol. Following three PBS washes, cells were lysed using RIPA buffer supplemented with protease/phosphatase inhibitors. After SDS-PAGE separation and PVDF membrane transfer, proteins were analysed with specific antibodies. Primary antibodies targeting NF-κB, as well as their phosphorylated forms, were obtained from Cell Signaling Technologies (Cambridge, MA). Detection was performed using ECL (Millipore), with the band intensity measured using ImageJ. The primary antibodies used in this study are listed in Table S2.

2.12 The LPS-induced mouse calvarial osteolysis model

All animal experiments were conducted in accordance with the guidelines approved by the Animal Research Committee of Shanghai Ninth People's Hospital (SH9H-2023-A91-1). In this study, twenty-four 6–8 week-old male C57BL/6 mice were randomly divided into four groups ($n = 6$) after acclimatization under pathogen-free conditions. The groups were designated as follows: control (PBS only), LPS (5 mg kg^{-1} LPS + 200 μL of PBS), LPS + low-dose G-CDs (5 mg kg^{-1} LPS + 200 μL of 50 μg mL^{-1} G-CDs), and LPS + high-dose G-CDs (5 mg kg^{-1} LPS + 200 μL of 100 μg mL^{-1} G-CDs). Treatments were administered every other day starting two days post-surgery for a total duration of two weeks. At the endpoint, calvariae were collected and fixed in 4% paraformaldehyde.

2.13 Micro-CT scanning and histomorphometric analysis

A square region of interest (ROI) centered at the intersection of the mid-coronal and sagittal sutures was defined on reconstructed micro-CT images for the measurement of bone mineral density (BMD) and bone volume/tissue volume (BV/TV). Following fixation, calvariae were decalcified in 10% EDTA (pH 7.4) for two weeks, paraffin-embedded, and sectioned for histological analyses, including H&E staining, TRAP staining, and immunohistochemistry. Stained sections were examined and imaged under a Leica microscope (Germany).

2.14 Statistical analysis

All quantitative data are expressed as mean ± SD from a minimum of three independent replicates. Statistical significance was determined using SPSS 25.0 software by applying unpaired two-tailed t-tests (for two groups) or one-way ANOVA with Tukey's *post hoc* test (for multiple groups) for parametric data and Mann–Whitney/Kruskal–Wallis tests for non-parametric data. All graphs were plotted using GraphPad Prism 10.1.2, with $*p < 0.05$, $**p < 0.01$, and $***p < 0.001$ denoting statistical significance.

3. Results and discussion

3.1 Characterization of G-CDs

The transmission electron microscopy (TEM) images show that the G-CDs have uniform sizes and good dispersion (Fig. 1A). The high-resolution TEM (HRTEM) images and the inset in Fig. 1B confirm that the G-CDs have good crystallinity, with a clear lattice spacing of 0.21 nm. Through the measurement and analysis of particle diameters in the TEM images, the diameters of G-CDs are mainly distributed in the range of 2.2–4.0 nm, among which the proportion of carbon dots with a diameter of approximately 3 nm is the largest (Fig. 1C). In the Fourier transform infrared (FTIR) spectrum of the G-CDs (Fig. 1D), the broad peaks observed in the range of 3000–4000 cm^{-1} correspond to the stretching vibrations of O–H, N–H, and C–H bonds, respectively. The absorption peaks at 1640 cm^{-1} and 1407 cm^{-1} are attributed to the C=O and C–N stretching vibrations of the amide group, respectively. The peak at 1385 cm^{-1} corresponds to the bending vibration of the –CH$_3$ group, while the peak at 1110 cm^{-1} is associated with the bending vibration of the C–O bond in ester and alcohol structures.

In the photoluminescence (PL) spectra of the G-CDs (Fig. 1E), a peak appears at around 525 nm as the excitation wavelength increases from 460 nm to 480 nm. The UV-Vis spectrum of the G-CDs exhibits an optimal absorption peak at 252 nm in the UV region, characteristic of the π–π* transition of the C=C bonds within the carbon core, while showing no significant absorption in the visible region (Fig. S1).

X-ray photoelectron spectroscopy (XPS) data (Fig. 1F) confirm that carbon (C), oxygen (O), and nitrogen (N) are the primary elements present in the G-CDs. In the XPS high-resolution spectra, the C 1s peak can be deconvoluted into C–C (284.8 eV), C–O/C–N (286.0 eV), and C=O (287.9 eV) components (Fig. 1G).[33] The O 1s spectrum can be divided into C–O (532.5 eV) and C=O (530.9 eV) peaks, respectively (Fig. 1H),[34,35] while the N 1s spectrum can be fitted to pyrrolic N (400.8 eV), amine N (399.9 eV), and pyridinic N (399.2 eV), respectively (Fig. 1I).[36]

3.2 Biocompatibility of G-CDs

When evaluating the use of nanomaterials for treating inflammatory osteolysis, their biocompatibility is a primary concern. Macrophages are pivotal in this context, serving as key inflammatory effector cells and precursors for osteoclasts, which form through the fusion of several macrophages.[37] We assessed the cellular compatibility of G-CDs with BMMs and the macrophage cell line RAW264.7. Various concentrations of G-CDs (0, 1, 5, 10, 50, 100, and 200 μg mL^{-1}) were co-cultured with RAW264.7 cells and BMMs, and the CCK-8 assay was employed to determine the maximum safe concentration. The
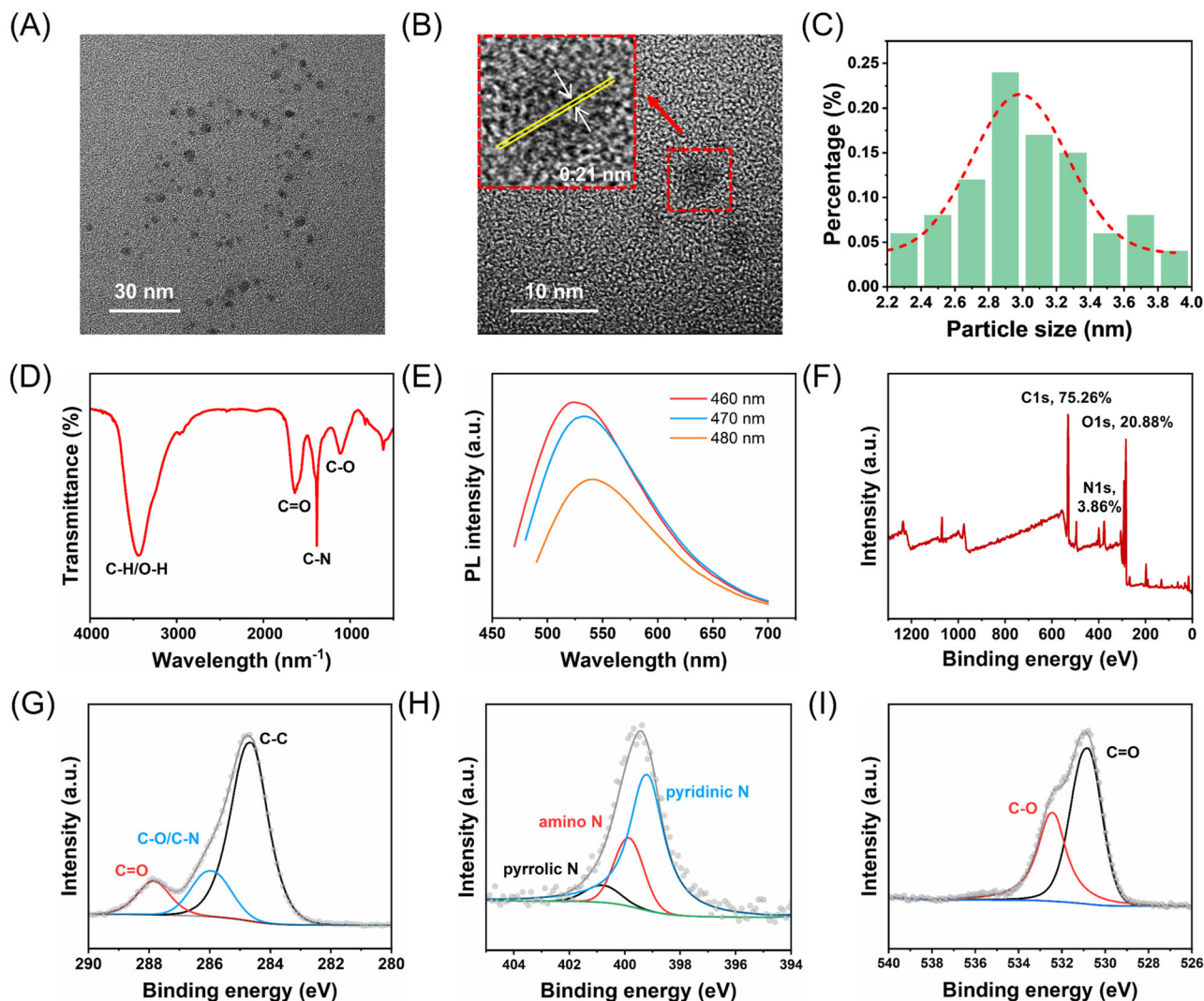
Fig. 1 Characterization of G-CDs. (A) TEM image, (B) HRTEM image, (C) particle size distribution histogram, (D) FTIR spectrum, (E) PL emission spectra at various excitation wavelengths, (F) full survey scan and high-resolution XPS spectra of (G) C 1s, (H) N 1s, and (I) O 1s.

results indicated that G-CDs were safe up to 100 μg mL^{-1} for both RAW264.7 cells and BMMs, confirming good biocompatibility (Fig. 2A and B). Consequently, concentrations of 50 and 100 μg mL^{-1} were selected for further experiments.

Owing to their small size and excellent biocompatibility, carbon dots (CDs) are capable of cellular internalization to exert their functions. To investigate whether G-CDs can be taken up by cells, we performed a cellular uptake assay. As shown in Fig. 2C, bright blue fluorescence was observed in RAW264.7 cells after 30 minutes of co-incubation with G-CDs, while no fluorescence was detected in the untreated control group. Furthermore, the fluorescence intensity within the cells exhibited a concentration-dependent increase, indicating that G-CDs are readily internalized by RAW264.7 cells.

3.3 Anti-inflammatory activity of G-CDs

The release of inflammatory mediators due to various factors is a primary cause of inflammatory osteolysis. Previous studies have shown that the combination of TNF-α and RANKL significantly stimulates the differentiation of osteoclasts and positively regulates the expression of osteoclast-specific mRNA markers.[38] Additionally, IL-6 mediates the stimulatory effects of TNF-α and enhances bone resorption by increasing the pool of osteoclastic progenitors and promoting their differentiation into mature osteoclasts.[39] Consequently, the main strategy for treating inflammatory osteolysis is to inhibit inflammation. In this study, we established a cell inflammation model using LPS-stimulated RAW264.7 cells and employed RT-qPCR to analyze the mRNA transcription levels of inflammation-related factors,[40] thereby investigating the effects of G-CDs on inflammation. The results demonstrated that LPS stimulation significantly upregulated the mRNA levels of inflammatory factors, including TNF-α, IL-6, IL-1β, and iNOS (Fig. 2D). Following the addition of G-CDs, the mRNA levels of these inflammatory factors were inhibited to varying degrees, with the high-concentration group exhibiting a greater inhibitory effect than the
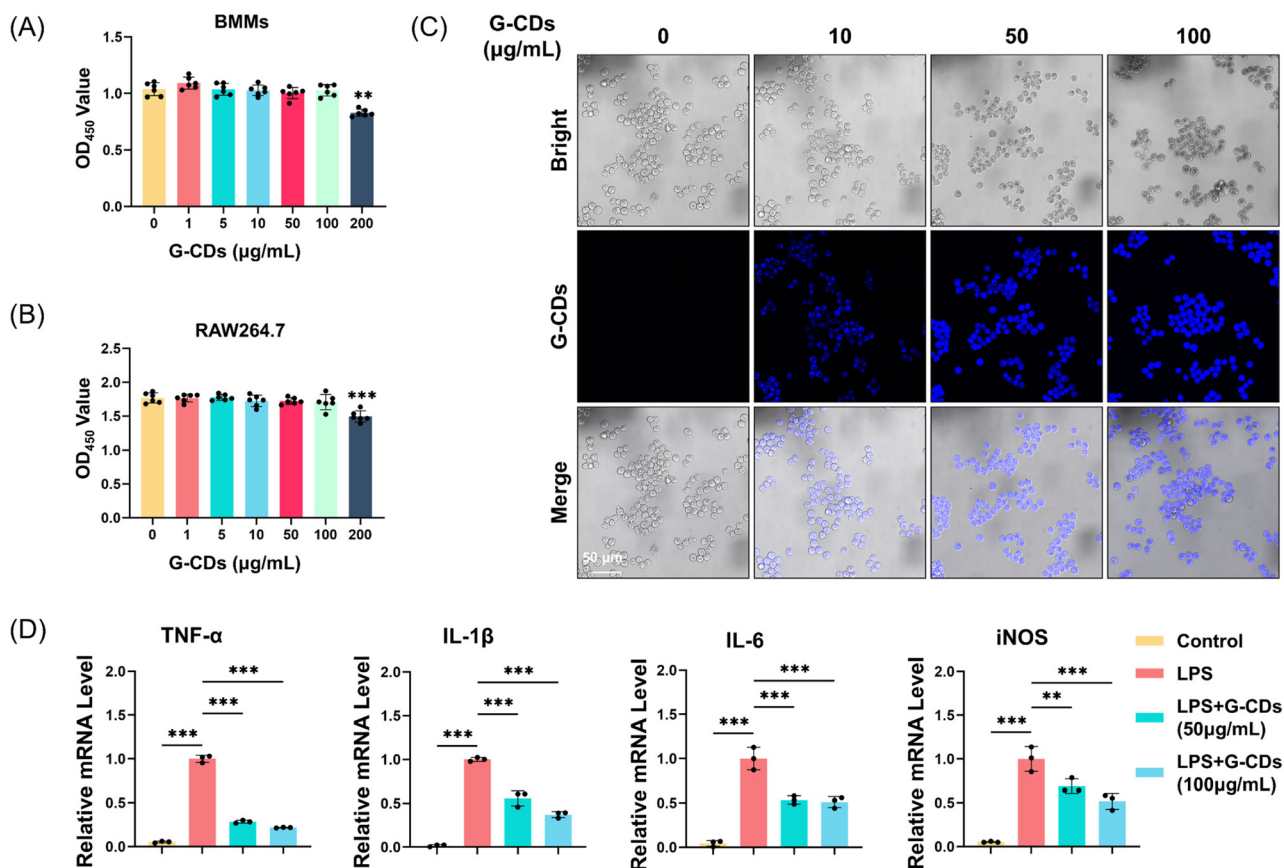
Fig. 2 Biocompatibility and anti-inflammatory activity of G-CDs. (A) Viability of BMMs and (B) RAW264.7 cells treated with G-CDs, as determined by the CCK-8 assay ($n = 6$). (C) Cellular uptake of G-CDs by RAW264.7 cells. (D) Relative mRNA expression levels of TNF-α, IL-1β, IL-6, and iNOS measured by RT-qPCR ($n = 3$).

low-concentration group. These findings indicate that G-CDs possess strong anti-inflammatory activity and can effectively inhibit the progression of inflammation.

3.4 Antioxidant activity of G-CDs

Redox imbalance is a pivotal pathological driver in inflammatory osteolysis.[7] Excessive ROS fuel a self-amplifying cycle: they activate NF-κB and MAPK pathways to potentiate RANKL-induced osteoclast differentiation, while simultaneously triggering the NLRP3 inflammasome to boost pro-inflammatory cytokines (TNF-α and IL-1β).[41] These cytokines further stimulate ROS generation, establishing a vicious feedback loop that exacerbates bone resorption. Consequently, disrupting this oxidative-inflammatory axis represents a promising therapeutic strategy.

To investigate the role of G-CDs as a redox regulator, we performed a series of biochemical and cellular assays. The TMB assay revealed potent peroxidase-like activity (Fig. 3A), indicative of H_2O_2 scavenging potential relevant to RANKL signaling inhibition. Consistently, G-CDs also exhibited SOD-mimetic activity in a cell-free environment (Fig. 3B). Remarkably, in RAW264.7 cells, G-CD treatment markedly elevated endogenous SOD activity (Fig. 3C). Consequently, this enhanced antioxidant capacity promoted effective ROS clearance (Fig. 3D

and E), leading to the suppression of inflammasome activation. H_2O_2 clearance impedes NF-κB/MAPK-dependent transcriptional activation of osteoclastogenic regulators while SOD-mediated ROS reduction mitigates cytokine-driven osteoclast differentiation. Consequently, G-CDs represent multi-target antioxidants capable of dismantling the ROS-inflammation feedback loop more effectively than single-action agents. Their concurrent targeting of upstream inflammasome activation and downstream RANKL signaling provides a mechanistic foundation for mitigating osteolytic progression. This antioxidant potency positions G-CDs as promising candidates for suppressing inflammatory bone loss prior to downstream cellular effects on osteoclasts.

3.5 Inhibition of RANKL-induced osteoclastogenesis by G-CDs

Osteoclast-mediated bone resorption is a pivotal pathological driver in inflammatory osteolysis. To systematically evaluate the therapeutic potential of G-CDs, we investigated their effects on RANKL-induced osteoclastogenesis in BMMs.[42] Under stimulation with M-CSF and RANKL, BMMs underwent fusion to form multinucleated osteoclasts, as unequivocally visualized by TRAP staining (Fig. 4A). Strikingly, G-CD treatment elicited a concentration-dependent suppression of osteo-
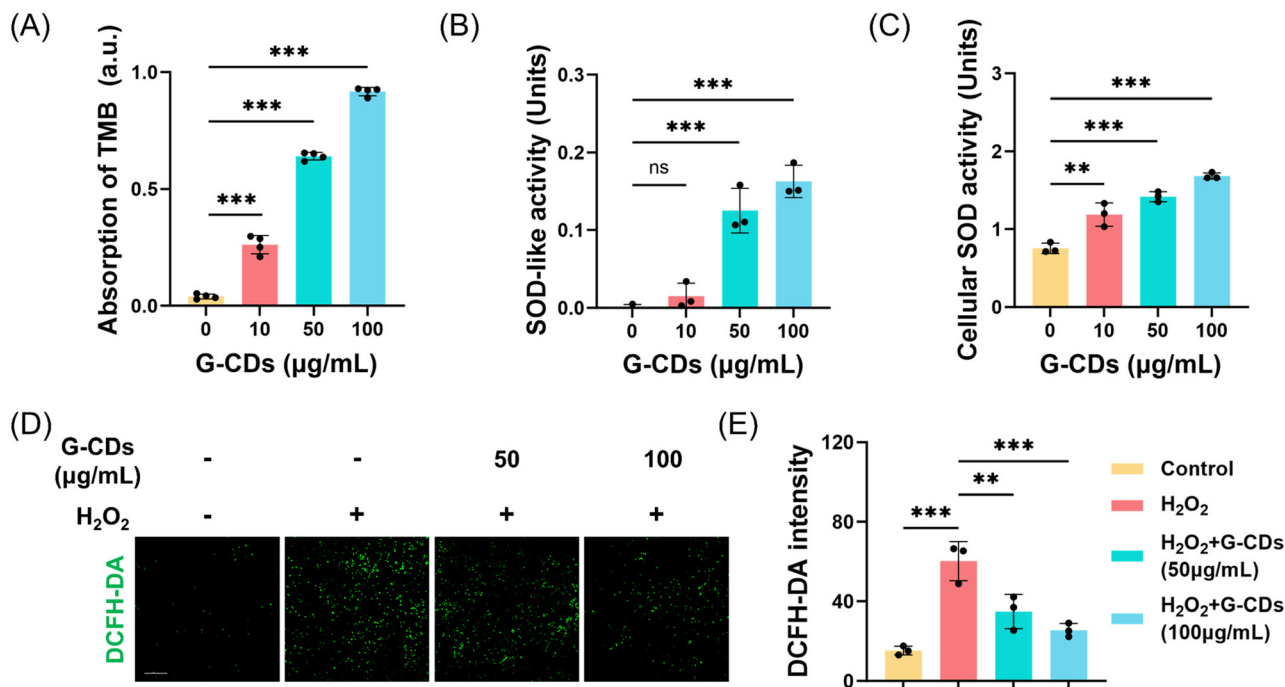
Fig. 3 Antioxidant activity of G-CDs. (A) Absorbance of TMB in the presence of G-CDs ($n = 3$). (B) SOD-like enzyme activity of G-CDs in a cell-free system ($n = 3$). (C) Intracellular SOD activity in RAW264.7 cells after treatment with G-CDs ($n = 3$). (D) Representative fluorescence images and (E) quantitative analysis of intracellular ROS scavenging by G-CDs, detected by the DCFH-DA assay ($n = 3$).

clast formation, significantly reducing both the size and number of TRAP$^+$ multinucleated cells (Fig. 4B and C).

To elucidate the molecular underpinnings of this inhibition, we profiled key osteoclastogenic genes *via* RT-qPCR. G-CDs markedly downregulated the expression of c-Fos and NFATc1 (Fig. 4D and E)—transcription factors governing the osteoclast differentiation cascade. c-Fos serves as an early master regulator upstream of NFATc1, while NFATc1, activated through RANKL signaling, orchestrates the expression of effector genes critical for osteoclast function. Mechanistically, G-CDs suppressed NFATc1-dependent transcriptional programs, notably reducing the expression of TRAP (required for bone demineralization), CTSK (mediates type I collagen cleavage), and DC-STAMP (a fusogenic protein pivotal for osteoclast multinucleation) (Fig. 4F–H).[43] This coordinated suppression of osteoclast-specific genes demonstrates that G-CDs disrupt osteoclastogenesis at the transcriptional level. Mechanistically, the inhibition of c-Fos and NFATc1 implies interference with the RANKL signaling axis, potentially impeding the activation of downstream resorptive programs. The reduction in DC-STAMP further substantiates the impaired cell fusion observed in TRAP staining. Collectively, our findings establish that G-CDs attenuate osteoclast differentiation by targeting both early transcriptional drivers (c-Fos/NFATc1) and terminal functional markers (TRAP/CTSK/DC-STAMP), positioning them as promising candidates for mitigating inflammatory bone loss.

The balance between osteoclastogenesis and osteogenesis is critical in the context of inflammatory osteolysis.[44] We next investigated the potential osteogenic effect of G-CDs on bone marrow mesenchymal stem cells (BMSCs). As shown in Fig. S2, alkaline phosphatase (ALP) staining revealed that G-CDs enhanced ALP activity in a concentration-dependent manner. This pro-osteogenic effect was further supported by RT-qPCR analysis, which showed that G-CDs upregulated the expression of key osteogenic markers, including ALP, RUNX2, OPN, and OCN (Fig. S3). Collectively, these findings indicate that G-CDs not only inhibit osteoclast differentiation but also promote osteogenic differentiation, thereby shifting the bone remodeling equilibrium toward bone formation.

3.6 Inhibition of F-actin ring formation by G-CDs

The resorptive function of osteoclasts hinges critically on their specialized cytoskeletal architecture. During bone resorption, mature osteoclasts establish sealed resorption compartments through the assembly of two interdependent structures: a peripheral actin ring that anchors the cell to the mineralized matrix and a central ruffled border that facilitates proton and protease secretion.[45] The actin ring itself is organized into densely packed podosomes—dynamic actin-rich protrusions conserved across invasive cell types. Unique to osteoclasts, however, is their reorganization into annular superstructures *via* interconnecting actin cables, forming a contiguous adhesion belt essential for creating the sealed microcompartment required for efficient bone degradation. Crucially, the formation of these filamentous actin (F-actin) rings serves as both a structural prerequisite and a functional hallmark of osteoclast maturation.
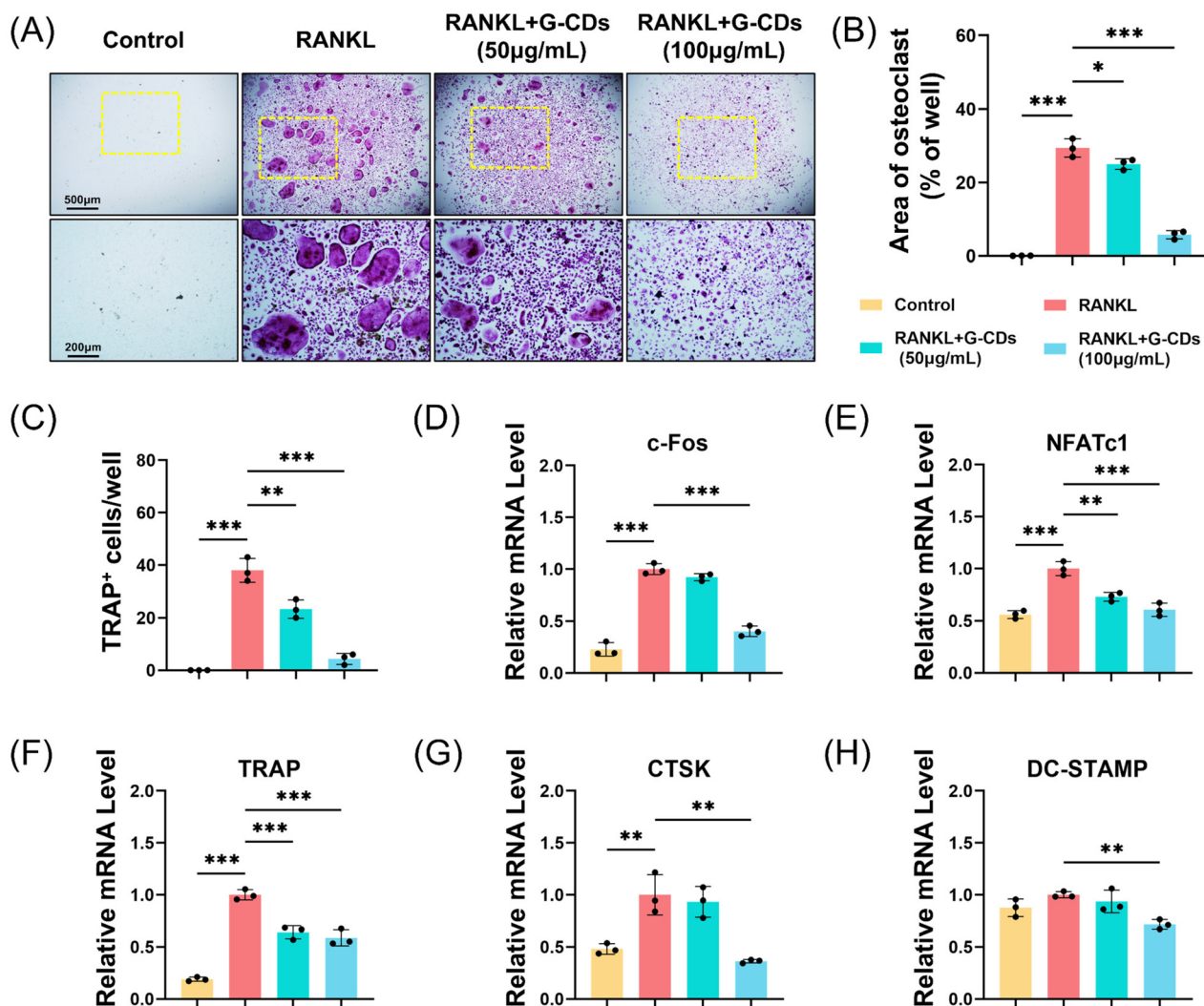
Fig. 4 G-CDs inhibit RANKL-induced osteoclastogenesis. (A) TRAP staining images of RANKL-mediated osteoclasts treated with or without G-CDs (scale bar = 500 μm; enlarged images scale bar = 200 μm). (B and C) Quantification of the area of osteoclasts and TRAP-positive cells (n = 3). (D–H) The mRNA expression levels of c-Fos, NFATc1, TRAP, CTSK, and DC-STAMP evaluated using RT-qPCR (n = 3), respectively.

To determine whether G-CDs impair this cytoskeletal remodeling process, we performed high-resolution immunofluorescence imaging of F-actin in RANKL-stimulated osteoclasts. Control osteoclasts derived from BMMs exhibited well-defined, circular F-actin rings (Fig. 5A), confirming successful cytoskeletal polarization. Strikingly, G-CD treatment profoundly disrupted this organization, manifesting as fragmented actin clusters or absent rings. Quantitative analysis revealed a significant reduction in both the number (Fig. 5B) and spatial coherence of F-actin structures, indicating defective cytoskeletal patterning.

Functionally, this morphological disruption compromised osteoclast activity, as evidenced by a direct correlation between diminished F-actin rings and a reduced cell spreading area (Fig. 5B), a surrogate for resorptive ability. We propose that the collapse of the actin cytoskeleton stems from G-CD-mediated inhibition of osteoclast fusion and/or interference with Rho

GTPase-driven actin polymerization, a key RANKL-NFATc1 downstream event. Ultimately, by dismantling the cytoskeletal machinery required for the sealing zone, G-CDs effectively inhibit the bone-degrading mechanism of osteoclasts.

3.7 Inhibitory effect of G-CDs on osteoclast bone resorption function

Osteoclasts execute physiological bone resorption in coordination with osteoblasts to preserve skeletal homeostasis.[46] Pathological overactivation of these cells however drives excessive bone degradation, underpinning disorders like osteoporosis and inflammatory osteolysis. Targeting osteoclast resorptive function thus represents a strategic therapeutic approach.

To evaluate G-CDs' impact on bone degradation capacity, we cultured BMMs on bovine bone slices under RANKL stimulation. Control osteoclasts generated profound resorption pits
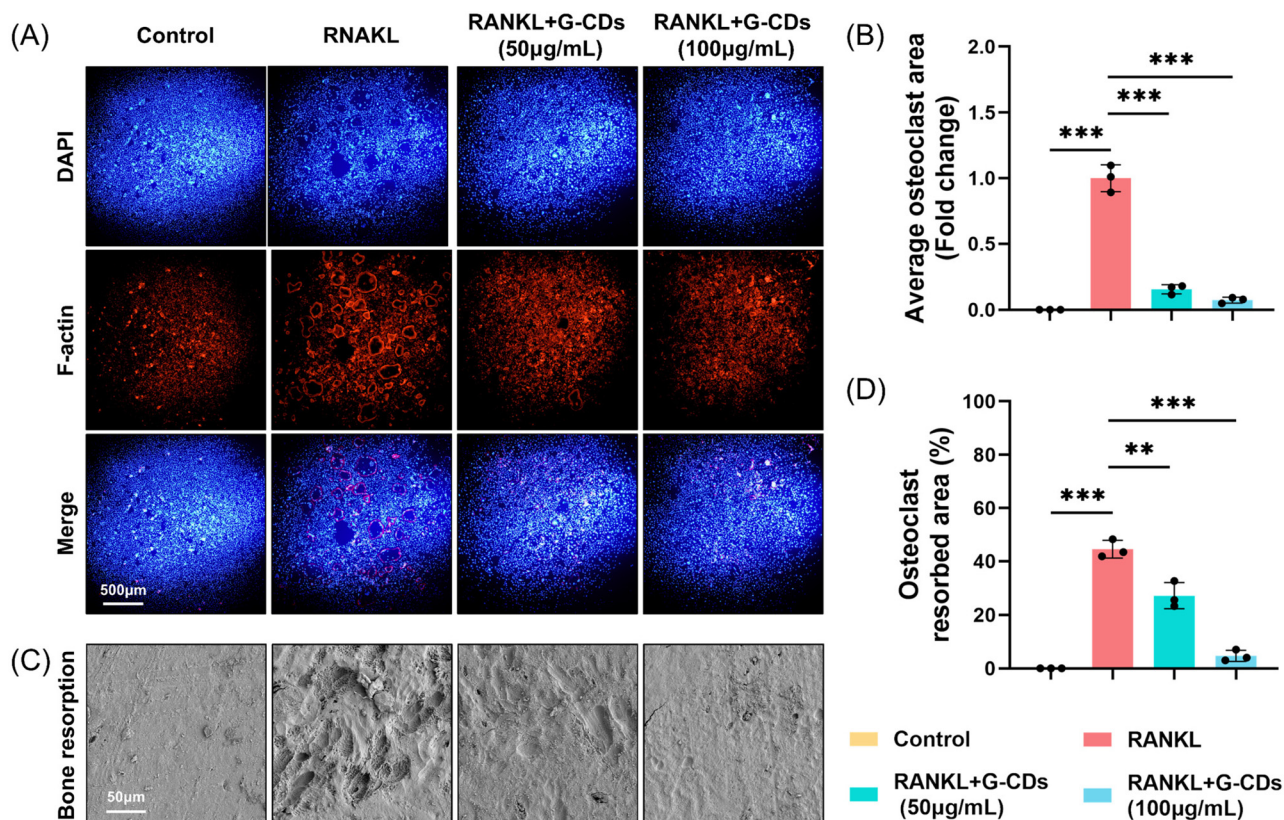
Fig. 5 The effect of G-CDs on RANKL-induced actin ring formation and resorptive function in osteoclasts. (A) Representative images showing F-actin formation (scale bar = 500 μm); F-actin belts: red, DAPI: blue. (B) Quantitative analyses on the average area of the osteoclast (n = 3). (C) Detection of the osteoclast resorption pits (scale bar = 50 μm). (D) Quantitative analysis of the resorption pit area (n = 3).

reflecting unrestrained resorptive activity (Fig. 5C). Strikingly, G-CD treatment markedly suppressed pit formation, reducing both their number and depth. Quantitative analysis confirmed a significant decrease in the resorption area (Fig. 5D), directly demonstrating impaired osteoclast function.

3.8 G-CDs inhibit osteoclast differentiation by suppressing NF-κB signaling

The impaired osteoclast function results from the multimodal action of G-CDs. They disrupt F-actin ring formation (Fig. 5A), compromising the sealing zone needed for bone resorption; suppress CTSK expression (Fig. 4G), reducing collagen degradation; and decrease cell spreading (Fig. 5B), limiting bone contact. Together, these effects inhibit resorption from acidification to matrix breakdown. The consistency among cytoskeletal, molecular, and functional readouts confirms a causal link between G-CDs and osteoclast dysfunction.

We next examined the NF-κB pathway, which is essential for RANKL-induced osteoclastogenesis. RANKL activates IKK, leading to IκBα phosphorylation and degradation, nuclear translocation of p65/p50, and transcription of osteoclastogenic genes such as NFATc1, TRAP, and CTSK.[7,47] In BMMs, G-CDs suppressed RANKL-induced phosphorylation of IκBα and p65 and attenuated IκBα degradation in a dose-dependent manner (Fig. 6A–C). By blocking IKK activity and stabilizing IκBα,

G-CDs prevent NF-κB nuclear translocation and inhibit downstream gene expression. This mechanism underlies the impaired osteoclast differentiation and resorption shown in Fig. 4 and 5.

RANKL stimulation strongly induced phosphorylation of IκBα and p65, confirming pathway activation. Importantly, G-CD treatment suppressed IκBα and p65 phosphorylation and attenuated IκBα degradation in a dose-dependent manner. By inhibiting IKK-mediated IκBα phosphorylation and stabilizing the cytoplasmic NF-κB complex, G-CDs prevent nuclear translocation of p65/p50. Consequently, transcriptional activation of downstream effectors—including NFATc1, TRAP, and CTSK—is compromised, directly explaining the impaired osteoclast differentiation and bone resorption, as shown in Fig. 4 and 5. These results demonstrate that G-CDs disrupt osteoclastogenesis primarily by inhibiting the NF-κB pathway at an early stage. Targeting this upstream step provides a therapeutic advantage over downstream inhibitors, as it simultaneously suppresses multiple osteoclastogenic genes regulated by NF-κB. The coherence among NF-κB inhibition, suppressed gene expression, cytoskeletal defects, and reduced bone resorption supports a clear mechanistic narrative. The ability of G-CDs to disrupt this pivotal pathway while retaining antioxidant properties underscores their multimodal potential for treating osteolytic diseases.
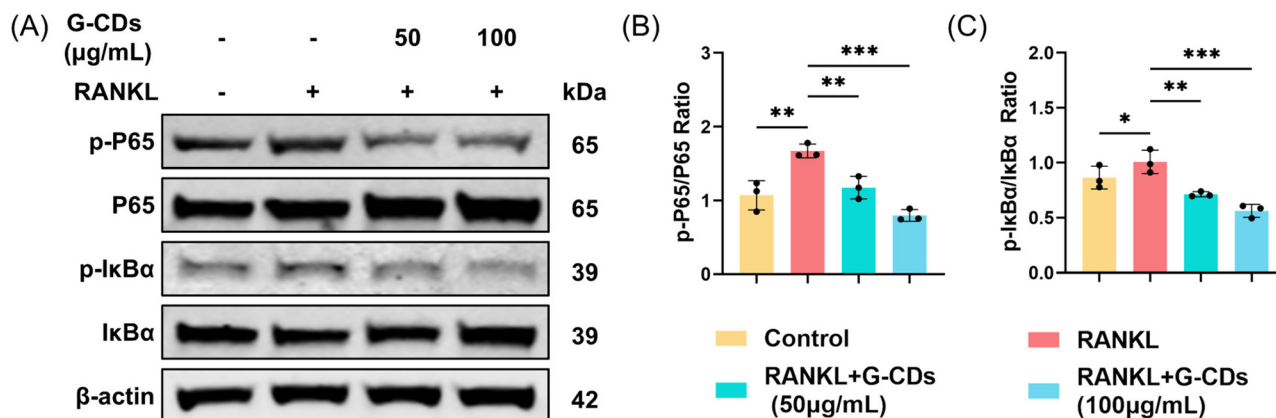
Fig. 6 G-CDs suppress RANKL–induced NF–κB signaling pathways in osteoclast differentiation. (A) The protein expressions of p-P65, P65, p-IκBα and IκBα were assessed by western blot. (B) The ratios of p-P65/P65 (n = 3). (C) The ratios of p-IκBα/IκBα (n = 3).

3.9 G-CDs inhibit LPS-induced inflammatory osteolysis *in vivo*

To investigate the protective effects of G-CDs against inflammatory osteolysis, we established an LPS-induced mouse calvarial osteolysis model. Micro-computed tomography (micro-CT) analysis provided three-dimensional structural evidence of bone destruction. As shown in Fig. 7A, the LPS group exhibited severe cranial bone erosion characterized by larger and deeper resorptive pits on the calvarial surface compared to the control group. Quantitative analysis further confirmed these morpho-

logical changes, with the LPS group showing significant reductions in both bone mineral density (BMD) and bone volume/tissue volume (BV/TV) ratio (Fig. 7B and C). Notably, G-CD treatment effectively attenuated LPS-induced bone resorption in a dose-dependent manner, with the high-dose group demonstrating nearly complete preservation of the bone microstructure.

Histopathological examination provided additional insights into the cellular mechanisms underlying bone protection. H&E staining revealed substantial bone loss and structural disruption in LPS-treated mice, while TRAP staining identified
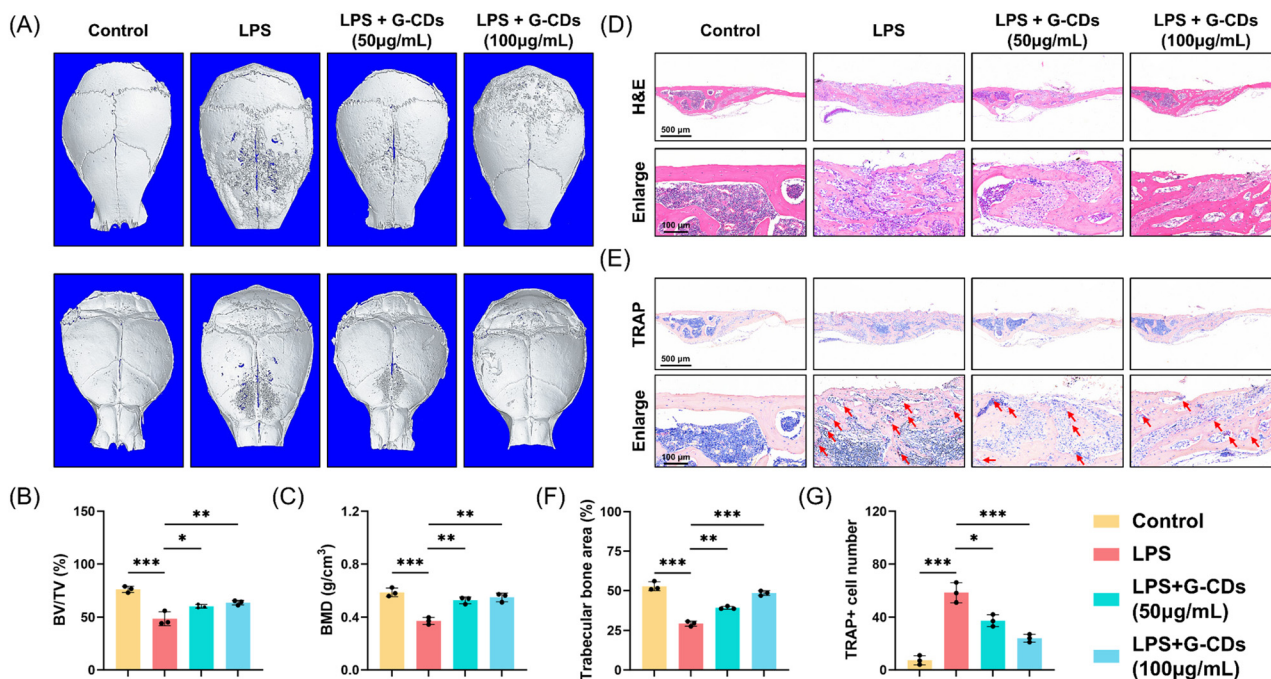

Fig. 7 G-CDs mitigate LPS-induced calvarial osteolysis *in vivo*. (A) Representative 3D micro-CT reconstruction images of mouse calvaria. (B and C) Morphometric analysis of the bone volume/total volume (BV/TV) ratio and bone mineral density (BMD) (n = 3). (D and E) Representative histological images of H&E and TRAP staining. (F and G) Quantitative analysis of the trabecular bone area from H&E-stained sections and the number of TRAP-positive osteoclasts (n = 3).

numerous multinucleated osteoclasts adhering to the eroded bone surfaces (Fig. 7D and E). These histological findings directly correlate with the excessive osteoclast activity driving inflammatory bone destruction. Importantly, G-CD administration resulted in a dose-dependent decrease in both bone erosion area and osteoclast number (Fig. 7F and G), consistent with the micro-CT observations.

The concordance between radiological and histological data collectively demonstrates the potent therapeutic efficacy of G-CDs against inflammatory osteolysis *in vivo*. Together with our preceding *in vitro* findings, these results position G-CDs as a highly promising nanotherapeutic agent for the treatment of inflammatory osteolytic diseases.

4. Conclusion

In summary, this study successfully developed ginger-derived carbon dots (G-CDs) through a facile and environmentally friendly hydrothermal method. The as-prepared G-CDs exhibited excellent water dispersibility, uniform size distribution, and favorable biocompatibility. More importantly, we systematically demonstrated their multifunctional therapeutic effects against inflammatory osteolysis through both *in vitro* and *in vivo* experiments. The G-CDs effectively scavenged reactive oxygen species, suppressed pro-inflammatory cytokine expression, and inhibited RANKL-induced osteoclastogenesis *via* suppression of the NF-κB signaling pathway. This molecular intervention led to the downregulation of key osteoclastogenic transcription factors (c-Fos and NFATc1) and functional genes (TRAP, CTSK, and DC-STAMP), ultimately disrupting F-actin ring formation and bone resorption activity. Notably, in an LPS-induced murine calvarial osteolysis model, G-CD administration significantly alleviated bone destruction in a dose-dependent manner. The concordance between anti-oxidant, anti-inflammatory, and anti-osteoclastogenic effects underscores the multimodal therapeutic potential of G-CDs. Our findings highlight the promise of plant-derived carbon dots as sustainable nanotherapeutics for treating inflammatory osteolytic disorders, offering a green alternative to conventional synthetic approaches while maintaining targeted bioactivity.

Conflicts of interest

We declare that there are no conflicts of interest associated with this publication.

Ethical statement

All animal procedures were performed in accordance with the Guidelines for Care and Use of Laboratory Animals of Shanghai Jiao Tong University School of Medicine and the national guidelines of China. The experiments were approved by the Animal Ethics Committee (Animal Research Committee) of the Ninth People's Hospital (approval no. SH9H-2023-A91-1).

Data availability

The data that support the findings of this study are available from the corresponding authors upon reasonable request.

Additional experimental results, PCR primer sequences, and antibody sources can be found in the Supplementary Information. See DOI: https://doi.org/10.1039/d5nr03158c.

Acknowledgements

References

1 G. Mbalaviele, D. V. Novack, G. Schett and S. L. Teitelbaum, *J. Clin. Invest.*, 2017, **127**, 2030–2039.

2 N. Komatsu and H. Takayanagi, *Nat. Rev. Rheumatol.*, 2022, **18**, 415–429.

3 R. Gruber, *J. Clin. Periodontol.*, 2019, **46**(Suppl 21), 52–69.

4 Q. Gu, H. Yang and Q. Shi, *J. Orthop. Transl.*, 2017, **10**, 86–93.

5 L. Chen, Z. Tong, H. Luo, Y. Qu, X. Gu and M. Si, *Int. J. Oral Sci.*, 2023, **15**, 49.

6 A. Khoshroo, K. Ramezani, N. Moghimi, M. Bonakdar and N. Ramezani, *Inflammopharmacology*, 2023, **31**, 689–697.

7 X. Shi, T. Gao, C. Yu, S. Fu, T. Guo, W. Xu, X. Li, Y. Wang, J. Zhang, X. Jia and Y. Mao, *Inflammopharmacology*, 2024, **32**, 3461–3474.

8 L. Wei, W. Chen, L. Huang, H. Wang, Y. Su, J. Liang, H. Lian, J. Xu, J. Zhao and Q. Liu, *Pharmacol. Res.*, 2022, **184**, 106400.

9 L. Xing, E. M. Schwarz and B. F. Boyce, *Immunol. Rev.*, 2005, **208**, 19–29.

10 J. Lam, Y. Abu-Amer, C. A. Nelson, D. H. Fremont, F. P. Ross and S. L. Teitelbaum, *Ann. Rheum. Dis.*, 2002, **61**(Suppl 2), ii82–ii83.

11 Z.-F. Wu, X.-X. Luo, X.-F. Shi, B.-J. Wang, H.-W. Sun, Z.-N. Sun, Y.-Q. Mao and H.-M. Xiong, *Nanoscale*, 2025, **17**, 4958–4973.

12 L. Jiang, H. Cai, W. Zhou, Z. Li, L. Zhang and H. Bi, *Adv. Mater.*, 2023, **35**, e2210776.

13 Z.-F. Wu, B.-J. Wang, J.-W. Ni, Z.-N. Sun, X.-R. Zhang and H.-M. Xiong, *Nano Lett.*, 2024, **24**, 9675–9682.

14 W.-J. Zheng, Z.-N. Sun, Y.-M. Wang and H.-M. Xiong, *Nano Res.*, 2024, **17**, 8495–8503.

15 Y. Liu, L. Zhang, H. Cai, X. Qu, J. Chang, G. I. N. Waterhouse and S. Lu, *Sci. Bull.*, 2024, **69**, 3127–3149.

16 X. Wang, T. Wu, Y. Yang, L. Zhou, S. Wang, J. Liu, Y. Zhao, M. Zhang, Y. Zhao, H. Qu, H. Kong and Y. Zhang, *J. Nanobiotechnol.*, 2023, **21**, 63.

17 Z.-F. Wu, Z.-N. Sun and H.-M. Xiong, *Chin. J. Chem.*, 2023, **41**, 2035–2046.

18 X. Wang, L. Liu, D. Liang, Y. Liu, Q. Zhao, P. Huang, X. Li and W. Fan, *J. Hazard. Mater.*, 2021, **415**, 125579.

19 X. Shi, Q. Ma, X. Jia, Z. Wu, C. Yu, T. Gao, W. Xu, Z. Sun, J. Zhang, H. Xiong and Y. Mao, *Small Struct.*, 2024, 2400435.

20 H. Ding, X.-X. Zhou, J.-S. Wei, X.-B. Li, B.-T. Qin, X.-B. Chen and H.-M. Xiong, *Carbon*, 2020, **167**, 322–344.

21 X. Niu, W. Zheng, T. Song, Z. Huang, C. Yang, L. Zhang, W. Li and H. Xiong, *Chin. Chem. Lett.*, 2023, **34**, 107560.

22 Z. Chen, S.-Y. Ye, Y. Yang and Z.-Y. Li, *Pharm. Biol.*, 2019, **57**, 498–506.

23 D. Li, K.-Y. Xu, W.-P. Zhao, M.-F. Liu, R. Feng, D.-Q. Li, J. Bai and W.-L. Du, *Front. Pharmacol.*, 2022, **13**, 815479.

24 Y. Liu, Y. Zhao, S. Guo, D. Qin, J. Yan, H. Cheng, J. Zhou, J. Ren, L. Sun, H. Peng, X. Wu and B. Li, *Carbohydr. Polym.*, 2024, **346**, 122656.

25 S. Chen, Q. Zeng, X. Tan, M. Ye, Y. Zhang, L. Zou, S. Liu, Y. Yang, A. Liu, L. He and K. Hu, *Carbohydr. Polym.*, 2023, **314**, 120938.

26 R. Zhang, X. Lin, R. Lin, Z. Chen, C. Miao, Y. Wang, X. Deng, J. Lin, S. Lin, S. Weng and M. Chen, *J. Nanobiotechnol.*, 2025, **23**, 58.

27 F. Li, T. Li, C. Sun, J. Xia, Y. Jiao and H. Xu, *Angew. Chem., Int. Ed.*, 2017, **56**, 9910–9914.

28 F. Ayustaningwarno, G. Anjani, A. M. Ayu and V. Fogliano, *Front. Nutr.*, 2024, **11**, 1364836.

29 L. He, H. Duan, X. Chen, Y. Chen, Q. Mo, J. Huang, H. Zhao, X. Yao, J. Chen and Z. Yao, *Food Res. Int.*, 2023, **166**, 112589.

30 N. Li, X. Li, L. Deng, H. Yang, Z. Gong, Q. Wang, D. Pan, S. Zeng and J. Chen, *Phytomedicine*, 2023, **109**, 154562.

31 M. F. Mahomoodally, M. Z. Aumeeruddy, K. R. R. Rengasamy, S. Roshan, S. Hammad, J. Pandohee, X. Hu and G. Zengin, *Semin. Cancer Biol.*, 2021, **69**, 140–149.

32 X. Shi, W. Xu, Y. Xue, D. Zhao, H. Lv, D. Han, Y. Mao and Z. Du, *Eur. J. Pharmacol.*, 2025, **1001**, 177759.

33 H. Zhang, Z. Luo, W. Deng, J. Hu, G. Zou, H. Hou and X. Ji, *Chem. Eng. J.*, 2023, **461**, 142105.

34 Z. Qin, W. Wang, M. Wen, R. Zhang, Q. Zhang, K. Li, J. Li, W. Yang and Y. Zhou, *Spectrochim. Acta, Part A*, 2020, **229**, 117859.

35 K. B. Yatsimirskii, V. V. Nemoskalenko, V. G. Aleshin, Yu. I. Bratushko and E. P. Moiseenko, *Chem. Phys. Lett.*, 1977, **52**, 481–484.

36 D. Hong, Y. Choi, J. Ryu, J. Mun, W. Choi, M. Park, Y. Lee, N.-S. Choi, G. Lee, B.-S. Kim and S. Park, *J. Mater. Chem. A*, 2019, **7**, 20325–20334.

37 Y. Sun, J. Li, X. Xie, F. Gu, Z. Sui, K. Zhang and T. Yu, *Front. Immunol.*, 2021, **12**, 778078.

38 G. Luo, F. Li, X. Li, Z.-G. Wang and B. Zhang, *Mol. Med. Rep.*, 2018, **17**, 6605–6611.

39 S. Kwan Tat, M. Padrines, S. Théoleyre, D. Heymann and Y. Fortun, *Cytokine Growth Factor Rev.*, 2004, **15**, 49–60.

40 H. Yao, Y. Du, B. Jiang, Y. Liao, Y. Zhao, M. Yin, T. Li, Y. Sheng, Y. Ji and M. Du, *Free Radicals Biol. Med.*, 2023, **207**, 48–62.

41 Q. Yu, H. Shi, Z. Ding, Z. Wang, H. Yao and R. Lin, *Cell Commun. Signaling*, 2023, **21**, 1.

42 B. M. El-Masri, C. M. Andreasen, K. S. Laursen, V. B. Kofod, X. G. Dahl, M. H. Nielsen, J. S. Thomsen, A. Brüel, M. S. Sørensen, L. J. Hansen, A. S. Kim, V. E. Taylor, C. Massarotti, M. M. McDonald, X. You, J. F. Charles, J.-M. Delaisse and T. L. Andersen, *Bone Res.*, 2024, **12**, 62.

43 T. Jiang, T. Xia, F. Qiao, N. Wang, Y. Jiang and H. Xin, *Int. J. Mol. Sci.*, 2023, **24**, 16175.

44 Y. Li, J. Ling and Q. Jiang, *Front. Immunol.*, 2021, **12**, 691013.

45 L. S. Holliday, L. P. de Faria and W. J. Rody, *Int. J. Mol. Sci.*, 2020, **21**, 158.

46 M. Zaidi, T. Yuen, L. Sun and C. J. Rosen, *Endocr. Rev.*, 2018, **39**, 701–718.

47 H. Tao, W. Li, W. Zhang, C. Yang, C. Zhang, X. Liang, J. Yin, J. Bai, G. Ge, H. Zhang, X. Yang, H. Li, Y. Xu, Y. Hao, Y. Liu and D. Geng, *Pharmacol. Res.*, 2021, **174**, 105967.